USE OF MODULUS MAPPING TECHNIQUE TO INVESTIGATE CROSS-SECTIONAL MATERIAL PROPERTIES OF EXTRACTED SINGLE HUMAN TRABECULAE

ONDŘEJ JIROUŠEK[a], DANIEL KYTÝŘ[a], PETR ZLÁMAL[a], TOMÁŠ DOKTOR[a], JOSEF ŠEPITKA[b], and JAROSLAV LUKEŠ[b]

[a] Academy of Sciences of the Czech Republic, Institute of Theoretical and Applied Mechanics, v.v.i., Prosecká 76, 190 00, Prague 6, [b] Czech Technical University in Prague, Faculty of Mechanical Engineering, Technická 4, 166 07 Prague 6, Czech Republic
jirousek@itam.cas.cz

Keywords: modulus mapping, trabecular bone, nanoindentation, micromechanical testing

1. Introduction

Overall material properties of trabecular bone are function not only of bone density and architecture, but they are strongly dependent on the tissue properties. These properties at level of individual trabeculae can be obtained using nanoindentation of polished larger blocks of trabecular bone, however, one cannot distinguish between superficial layers and core of the trabecula where the properties are expected to differ[1].

The only study that uses nanoindentation of individual trabeculae in their cross-sections is the study by Brennan el al.[1], however, the properties were measured only in three distinct areas (core, middle, outer) and the authors used quasi-static nanoindentation. To our knowledge, modulus mapping (MM) has not been applied to measure properties of trabecular bone.

In their pioneering work[2], Asif et al. used modulus mapping to measure elastic properties of a carbon fiber epoxy composite. MM has been used to measure the nanoscale elastic properties of the collagen fibers, fibrils and mineral deposits in extrafibrillar space[3] in order to evaluate properties of nanocomposite films to mimic the hierarchy of natural bone. Recently the technique was used to measure the local variations in dentin and enamel in human teeth[4] but no verification with other experimental method has been done.

This study aims for the first time to investigate the local variations in material properties of single human trabecula in its cross-section. Average material properties obtained using MM technique are compared to elastic modulae measured by micromechanical testing.

2. Materials and methods

Thin and straight trabeculae (n=5, n – number of specimens) were located in a thin slice of trabecular bone extracted from proximal femur under magnification glass (4×). First, the samples were subjected to micromechanical testing and then modulus mapping procedure was performed.

Micromechanical tests

The trabeculae were tested in tension (n=3) and in three-point bending (n=2) to determine elastic modulae, yield strains and yield stresses. For tensile experiments, ends of the extracted trabeculae were embedded in epoxy resin. Samples were glued in custom tension-compression loading device, specially designed for these deliberate mechanical tests. For the three-point bending tests, no gluing was necessary and the samples were carefully placed on supports made of thin metal sheets.

Positioning of the samples as well as loading was provided by means of stepper motors and precision linear stages (UMR-3.5, Newport Corp, Irvine, CA). Deforming samples were recorded using a high-resolution CCD camera (CCD-1300F, Vosskuhler GmbH, Germany). Magnification was provided by an optical microscope (Navitar Imaging Inc., USA). Design of the experimental setup is shown in Fig. 1.

The samples were tested until complete fracture occurred. From the recorded images, displacements were evaluated using Lukas-Kanade tracking algorithm[5,6]. From the displacements, strains were calculated and complete stress-strain diagram was ascertained for each tested sample.
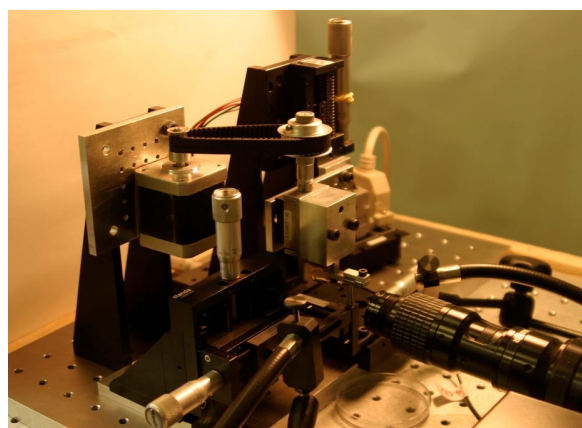

Fig. 1. **Experimental setup for micromechanical testing of isolated trabeculae (three point bending)**

The broken samples were then scanned in scanning electron microscope to quantify the damaged volume and later embedded in a low shrinkage epoxy resin, polished with diamond discs with decreasing grain sizes to reach the surface roughness of 20 nm to reveal the cross-section in undamaged part of trabecula. Detailed description of the sample preparation process can be found in a paper by Dudíková et al[7]. Example of cross-sectional image of the polished sample is depicted in Fig. 2.

Fig. 2. **Cross-section of trabecula embedded in epoxy resin. Image acquired by optical microscopy**

Modulus mapping procedure

To measure elastic properties in a larger area (35×35 μm) of trabecula's cross-section, modulus mapping technique (combination of dynamic mechanical analysis – nanoDMA and *in-situ* scanning probe microscopy – SPM) was applied in samples' undamaged parts. In this process, the probe is sinusoidally oscillating over the polished surface with a given frequency and load. From the recorded displacement amplitude and phase lag storage and loss modulae are determined.

During MM a small sinusoidal force is superimposed on top of a larger quasi-static force. Motion of the vibrating system of indenter and the surface sample can be described by equation of motion for one degree of freedom. Harmonic equation describing the motion is:

$$F_0 \sin(\omega t) = m\,\ddot{x} + c\,\dot{x} + kx \tag{1}$$

in which F_0 is the magnitude of the harmonic force, ω is the circular frequency of the system, c is the damping coefficient and k is the stiffness of the system. The system is assumed to be linear viscoelastic.

Denoting C_i stiffness of the indenter, C_s stiffness of the sample and A_0 amplitude of the system's response, we can write following equation for the time evolution of the dynamic response:

$$A_0 = \frac{F_0}{\sqrt{\left(k - m\omega^2\right)^2 + \left[\left(C_i + C_s\right)\omega\right]^2}} \tag{2}$$

Denoting $k = k_s + k_i$ (k_s is stiffness of the sample, k_i is stiffness of the indenter and k is the total spring stiffness) we can calculate the phase difference φ between the force and displacement from:

$$\tan\varphi = \frac{\left(C_i + C_s\right)\omega}{k - m\omega^2} \tag{3}$$

Prior the measurement, a dynamic calibration of the system is performed to establish three parameters of the system (indenter mass m, damping coefficient of the capacitive displacement sensor C_i, stiffness of the indenter k_i), leaving only stiffness k_s and damping coefficient C_s of the sample as unknown values.

In indentation, the contact stiffness k_s is proportional to the projected contact area A_c:

$$k_s = 2E^*\sqrt{\frac{A_c}{\pi}} \tag{4}$$

Using this, storage modulus *E'*, loss modulus *E''* and phase shift between the force and displacement δ can be calculated using following equations:

$$E' = \frac{k_s\sqrt{\pi}}{2\sqrt{A_c}}, \quad E'' = \frac{\omega C_s\sqrt{\pi}}{2\sqrt{A_c}}, \quad \tan\delta = \frac{\omega C_s}{k_s} \tag{5}$$

From the storage and loss modulae, complex modulus *E** can be computed using:

$$E^* = E' + iE'' \tag{6}$$

Comparison with quasi-static nanoindentation

Modulus mapping provides information about storage and loss modulae in a 256×256 square matrix. In our experiments, this matrix represented physical area 35×35 μm). To compare results from MM technique with quasi-static indentation, each sample was indented with a set of 9 indents in the center of the area used for MM.

In quasi-static indentation, maximal force 1000 μN was applied in 5 s loading part, which was followed by 5 s holding part, finally finished with 5 s unloading part. Nanoindentation curves, i.e. plots of force to depth for sample No. 4 are depicted in Fig. 3.

3. Results

Five samples have been successfully tested using micromechanical tests, modulus mapping and quasi-static nanoindentation. For nanoindentation, Poisson's number equal to 0.32 (ref.[8]) was considered.
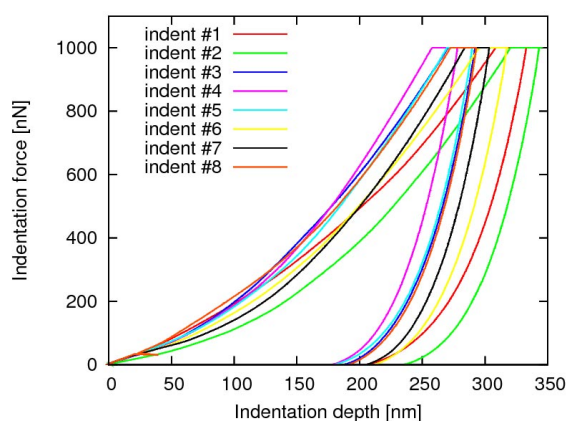
Fig. 3. **Example of the indentation curves from quasi-static indentation of sample No. 4**

Fig. 5. **Typical topography of the surface sample acquired by in-situ SPM (dimensions of scanned area 35×35 µm; sample No. 4)**

Young's modulae obtained from quasi-static indentation were in good correlation with results from micromechanical testing.

In every sample, matrices with loss modulae, storage modulae and tan delta (see Fig. 4) were stored. From these matrices, complex modulae were computed using equations (*5*) and (*6*).

To compare the MM technique to quasi-static nanoindentation, average values of complex modulae were determined for each sample. This required interpolating

the complex modulae with a smooth surface and extrapolating the values to the region representing the whole cross-section of the sample.

We used this technique to study the variations in material properties in the cross-section of the trabecuale. Results were showing similar trend to the findings published by Brennan et al.[1], i.e. the stiffness is highest in the core section of the trabecula and toward its surface it is decreasing. However, for two samples it was not possible to fit smooth surface through the values of complex modulae due to the large size of the samples compared to the relatively small area used for modulus mapping. Average values of the modulae are summarized in Tab. II and compared to the values obtained from micromechanical tests and from static nanoindentation.

In the table, values denoted by E_{mm} represents average values of complex modulae after fitting the smooth surface through the data and integrating the values over the whole cross-section. Values denoted by E_{qs} are average values

Table I
Average values of reduced and elastic modulae obtained by quasi-static indentation

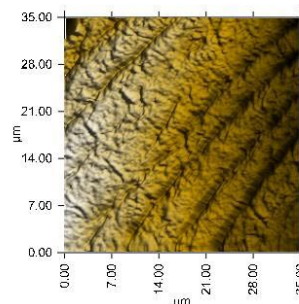| Sample No.	Reduced modulus [GPa]	Young's modulus [GPa]
1	13.26	12.04
2	17.48	15.93
3	17.79	16.22
4	19.52	17.82
5	19.62	17.91
6	13.29	12.07

Fig. 4. **Image maps of (a) complex modulus, (b) loss modulus and (c) storage modulus for sample No. 4**

Table II
Young's modulae (in GPa) obtained by modulus mapping (E_{mm}), quasi-static nanoindentation (E_{qs}) and from micromechanical testing ($E_{µm}$)

Sample	1	2	3	4	5	6
E_{mm}	--*)	14.17	14.91	16.90	--*)	13.29
E_{qs}	12.04	15.93	16.22	17.82	17.91	12.07
$E_{µm}$	10.71	14.61 #)		15.87	9.5**)	11.60

*) For these samples it was not possible to extrapolate a smooth surface over the whole cross-section, #) samples 2 and 3 represents two surfaces prepared for nanoindentation from one sample used in micromechanical testing, **) this value is influenced by overestimation of the cross-sectional area of the sample, see discussion in Jiroušek at al.[9]

obtained by quasi-static nanoindentation and finally $E_{\mu m}$ are elastic modulae measured by micromechanical testing.

4. Conclusions

Comparison of elastic properties obtained from micromechanical testing and modulus mapping technique was determined for each sample. After MM analysis, each sample was also tested using quasi-static nanoindentation.

Local variations in elastic properties were determined in cross-section of each sample using MM technique. Correlation between average elastic properties in cross-section and properties from micromechanical tests was found for all tested samples. Modulus mapping shows the trend of larger stiffness in core, smaller values are measured in superficial areas.

Both quasi-static nanoindentation and MM can be used to measure the elastic properties of extracted trabeculae, however, to identify material constants for more complicated material model (e.g. von Mises plasticity with kinematic hardening) it is necessary to use micromechanical testing.

REFERENCES

1. Brennan O., Kennedy O. D., Lee T. C., Rackard S. M., O'Brien F. O.: J. Biomech. *42*, 498 (2009).
2. Asif S. A., Wahl K. J., Colton R. J., Warren O. L.: J. Appl. Phys. *90* (3), (2001).
3. Khanna R., Katti S. K., Katti D. R.: Acta Biomater. *7*, 1173 (2011).
4. Balooch G., Marshall G. W., Marshall S. J., Warren O. L., Asif S. A. S., Balooch M.: J. Biomech. *37*, 1223 (2004).
5. Lucas B. D., Kanade T.: *Proc of Image Understanding Workshop*, 121–130, (1981).
6. Jiroušek O., Jandejsek I., Vavřík D.: J. Instrumentation *6*, C01039, (2011).
7. Dudíková M., Kytýř D., Doktor T., Jiroušek O.: Chem. Listy *105*, s790 (2011).
8. Ladd A. J. C., Kinney J. H.: J. Biomech. *31*, 941 (1998).
9. Jiroušek O., Kytýř D., Kunecký J., Zlámal P., Doktor T., Němeček J.: Chem. Listy *105*, s668 (2011).

O. Jiroušek[a], D. Kytýř[a], P. Zlámal[a], T. Doktor[a], J. Šepitka[b], and J. Lukeš[b] (*[a] Academy of Sciences of the Czech Republic, Institute of Theoretical and Applied Mechanics, Prague, [b] Czech Technical University in Prague, Faculty of Mechanical Engineering, Prague, Czech Republic):* **Use of Modulus Mapping Technique to Investigate Cross-Sectional Material Properties of Extracted Single Human Trabeculae**

This study aims to investigate the local variations in material properties of single human trabecula in its cross-section. Thin and straight trabeculae were located in a thin slice of trabecular bone extracted from proximal femur. Tensile and three-point bending tests were performed to determine elastic modulae, yield strains and yield stresses. To determine local variations in elastic properties in trabecula's cross-section, modulus mapping (MM) technique was applied in samples' undamaged parts. Using MM the storage and loss modulae are determined. Correlation between average elastic properties in cross-section and properties from micromechanical tests was found for all tested samples.

INVESTIGATION OF DIAMOND LIKE CARBON COATING DEPOSITED ON PLASMA NITRIDED AUSTENITIC STAINLESS STEEL

ZDENĚK JOSKA, JAROMÍR KADLEC, VOJTĚCH HRUBÝ, QUANG DUNG TRAN, and ZDENĚK POKORNÝ

Department of Mechanical Engineering, University of Defence in Brno, Kounicova 65, 662 10 Brno, Czech Republic
joska.zdenek@email.cz

Keywords: duplex coating, DLC coating, plasma nitriding, microhardness, adhesion

1. Introduction

Austenitic stainless steel AISI 316L is one of the most spread austenitic stainless steel, due to excellent corrosion resistance, superior cryogenic properties, good high-temperature strength, for these properties, it is used in the food and chemical industry and in medicine for surgical instruments[1]. But strong limitation as low wear resistance and poor hardness defend their applications. Duplex surface system was applied to improve surface and subsurface properties. The combination of both plasma nitriding and subsequent deposited thin film Diamond Like Carbon (DLC) were used as duplex treatment. Plasma nitriding is very universal treatment was used for creation of super-saturate austenite layer[2–4]. This layer is non magnetic, it has very high hardness and good corrosion resistance. High hardness, chemical inertness and excellent tribological properties of amorphous carbon coatings often called diamond-like carbon (DLC) coatings, are of great interest for technological applications[5,6]. When these coatings are deposited on soft substrate material due to their very thin thickness, further increase in the wear and especially in the load-bearing resistance is limited by plas-

tic deformation of the substrate, which results in the eventual collapse of the coating. In case of austenitic stainless steel plasma nitrided layer can created very useful transition layer between soft substrate and very hard thin coating[7–9]. The duplex treatment consisted of a plasma nitriding at 510 °C for 6 hours and subsequent coating with DLC layer was applied on AISI 316L stainless steel. The article is concerned to a study of the chemical composition and mechanical properties of duplex system.

2. Experimental material, methods and surface treatment

Samples of an AISI 316L stainless steel in the untreated state had the diameter of 30 mm and a thickness of 7 mm. The substrate had a microhardness of about 230 HV. Before the plasma nitriding process, the samples were wet ground using silicon carbide paper from 120 down to 4000 grit and finally polished with 1 μm diamond paste. Plasma nitriding was carried out in PN 60/60 Rübig equipment with these parameters: temperature of 510 °C, duration 6 h, pressure 320 Pa, gas mixture of H_2 flow 8 l/min and N_2 flow 24 l/min, pulse length 100 μm, voltage 520 V. The pre-nitrided samples were afterwards coated with DLC coatings in PVD industrial equipment HTC 625 Hauser. Depth profiles of plasma nitrided layers and PVD coatings were measured by GDOES/QDP method. GDOES measurements were performed in a LECO SA-2000. Calibration of nitrogen: JK41-1N and NSC4A standards. Confocal laser microscope LEXT OLS 3000 was used for observation of the cross section morphology of duplex coatings and craters after adhesion Rockwell tests. The surface hardness of duplex systems was evaluated by a Vickers microhardness test in a LECO automatic microhardness tester LM 247 AT. Surface microhardness was measured in range of load 0.1 N to 9.81 N. For each load, there were
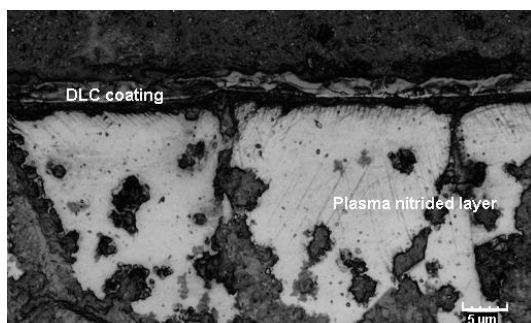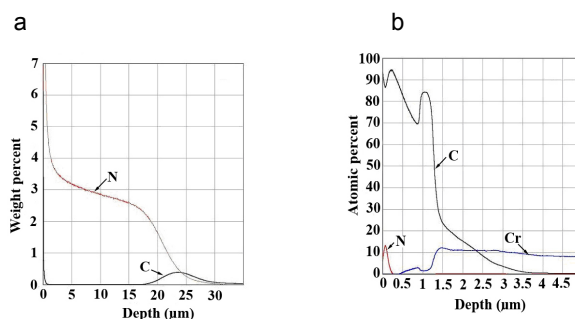

Fig. 1. **The chemically etched (by aqua - regia) cross-section showing the morphology of the duplex coating in a confocal micrograph**

2. **GDOES depth profile of a) plasma nitrided layer b) DLC coating on nitrided surface**

made 5 measurements and the resulting value is the average of these. Adhesion test was performed on the duplex coatings as a standard Rockwell test, while using a load of 1471 N and a diamond Rockwell indenter of 0.2 mm in diameter to assess the vertical adhesion of the coatings.

4. Experimental results

Fig. 1 shows an optical micrograph of a cross-section of the surface of an AISI 316L sample treated by a combination of a plasma nitriding and a PVD coating. The plasma nitriding process created a nitrided layer of 25 μm thickness. The DLC coatings subsequently deposited by PVD have the thickness of 1.5 μm. Depth profiles of the plasma nitrided layer (Fig. 2a) for both carbon and nitrogen are in good agreement with the proposed plasma treatment schedule. Carbon and nitrogen contents decrease along the layer depth (from surface to substrate). For carbon concentration there is a local maximum twenty micrometers from the surface. In the DLC coating on nitrided surface (Fig. 2b) carbon concentration gradually decreases to local maximum in depth 1 μm and decreased to zero value in the substrate. Indentation adhesion tests were performed by Rockwell indentation test (Fig. 4). The sample shows good adhesion in range HF1, without any delamination of coatings. The surface hardness of duplex treated samples (Fig. 3) showed that the highest values 3400 $HV_{0.01}$ were found in the duplex treated sample with the DLC coating. The single coated sample reached only 1700 $HV_{0.01}$.

5. Conclusion

Duplex surface treatment consisted of deposition of a plasma nitrided layer and subsequently deposition of a DLC coating. The analysis carried out by using GDOES/QDP method was in a good agreement with observation of the metallographic cross-section and microhardness measurement. The thickness of the nitrided layer was 25 μm and microhardness values were around 1150 $HV_{0.05}$. The surface hardness of duplex coatings reached
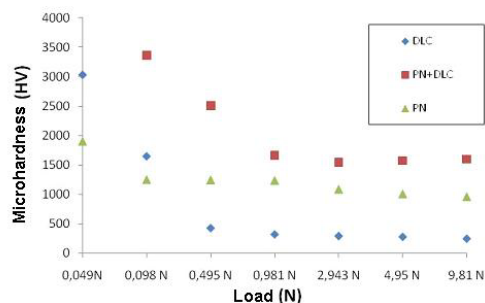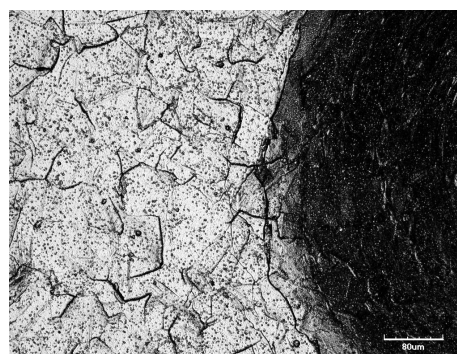

Fig. 4. **Rockwell indentation test of duplex coating**

3400 $HV_{0.01}$. Rockwell adhesion test shows that the plasma nitrided layer contributes to good adhesion of the DLC coating, which has then better adhesion than on a non-nitrided substrate.

REFERENCES
1. Lo K. H., Shek C. H., Lai J. K. L.: Mater. Sci. Eng. R: Reports. *65*, 4 (2009).
2. Kadlec J., Dvorak M.: Strenght of Materials. *40*, 118 (2008).
3. Czerwiec T., Renevier N., Michel H.: Surf. Coat. Technol. *131*, 267 (2000).
4. Pokorny Z., Kadlec J., Hruby V., et al.: Advances in Military Technology *6*, 1 (2011).
5. Jelinek M., Kocourek T., Kadlec J., Bulir J.: Laser Physics *13*, 10 (2003).
6. Jelinek M., Kocourek T., Bulir J., Novotny M., et al.: Laser Physics *15*, 2 (2005).
7. Joska Z., Kadlec J., Hruby V., et al.: Key Eng. Mater. *465*, (2011).
8. Heras E. De Las, Egidi D. A., Corengiea P., et al: Coat. Technol. *202*, 13 (2008).
9. Joska Z., Pospichal M., Mrazkova T., et al.: Chem. Listy *104*, S (2010).

Z. Joska, J. Kadlec, V. Hrubý, Q. Dung Tran, and Z. Pokorný *(University of Defence Brno):* **Investigation of DLC Coating Deposited on Plasma Nitrided Austenitic Stainless Steel**

In this article a duplex treatment was investigated. Duplex treatment consists of plasma nitriding and deposition of a DLC coating on AISI 316L stainless steel. This study covers the microstructure, chemical composition and mechanical properties of this duplex system. Analysis and discussion of the results showed that combination of these two processes improves considerably the surface hardness.

Fig. 3. **Surface microhardness of treated samples**

EVOLUTION OF STRUCTURE DURING LOCAL PLASTIC DEFORMATION IN Fe-Ni-B METALLIC GLASS

ALENA JURÍKOVÁ, KORNEL CSACH, and JOZEF MIŠKUF

Institute of Experimental Physics, Slovak Academy of Sciences, Watsonova 47, 040 01 Košice, Slovakia
akasard@saske.sk

Keywords: local plastic deformation, shear band, structural relaxation, amorphous alloy

1. Introduction

Metallic glasses have an attractive combination of mechanical and other physical properties. These materials can be prepared by rapid cooling of melt with proper composition. In the as-quenched alloy a significant amount of free volume is frozen due to the non-equilibrium processing conditions. As the periodical long-range order is absent in these materials, the creation and propagation the narrow shear bands with the thickness of cca 20 nm is the only micromechanism of the plastic deformation. The shear band creation is carried out under adiabatic conditions, and intensive local heating and subsequent rapid cooling cause the increase of the atomic disordering and the free volume creation[1]. The structure of amorphous alloys is influenced by the free volume amount and the structural relaxation is related to the free volume annihilation. Differential scanning calorimetry (DSC) analysis is the effective method to characterize the structural changes in amorphous materials. In the work we studied the local deformation-induced structural changes in the Fe-Ni-B amorphous ribbon.

2. Experimental

The specimens of the amorphous metallic ribbon $Fe_{40}Ni_{41}B_{19}$ with the thickness of 17.3 μm were annealed inside the tube furnace at the temperature of 200 °C for 2 hours in a flowing nitrogen atmosphere to anneal-out the quenched-in free volume. The structure of the annealed amorphous alloy was modified by the local plastic deformation performed by repeated impactions of a small hammer of 200 g with a tip of 1 mm radius, similar to ref.[2]. The impactions were randomly distributed through the both sides of ribbon samples. The accumulated deformation was characterized by the total number of these impactions per unit area of the sample. In this way the samples with different deformations were obtained (sample 1 – 160 impactions per 1 cm^2, 2 – 240/cm^2, 3 – 320/cm^2 and 4 – 640/cm^2). The enthalpy changes were measured using DSC 8000 calorimeter in two subsequent runs up to the temperature of 350 °C at a heating rate of 20 °C/min in a flowing nitrogen atmosphere. The third run was measured up to 520 °C (above the crystallization temperature). For characterization of structural changes, the differences between the first and the second runs were used.

3. Results and discussion

Fig. 1 shows representative DSC thermograms for the as-quenched sample up to the temperature of 520 °C. The dominant narrow exothermic peak with maximum at 442 °C corresponds to the transition from the amorphous to the crystalline phase. The enlarged portion of the DSC traces depicted by dash-line box for repeated heating up to 350 °C (with saved amorphous structure) can be seen in the insert of Fig. 1. At the temperatures above 140 °C the small enthalpy changes associated with irreversible structural changes occur. This thermal effect is connected with an annihilation of the excess free volume during structural relaxation in the amorphous state.

Repeated tip impactions on the annealed sample surface led to the local plastic deformation of the amorphous ribbon through the creation of narrow shear bands. The typical shear band morphology of a deformed specimen can be seen in Fig. 2. The plastic deformation in complex geometrical conditions occurs via sliding along the shear bands in different directions. Similar morphology of the deformed surface has been observed for other metallic glasses[3,4]. The total deformation energy is stored into the volume of narrow shear bands and into the regions of elastic deformation outside the bands. The structure of the
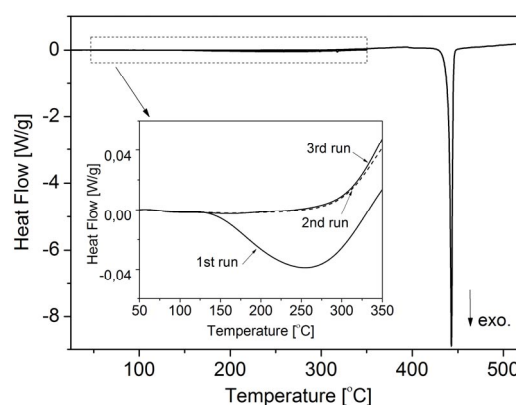

Fig. 1. **DSC scans of Fe-amorphous alloy in the as-quenched state in three subsequent heating runs. The enlarged portion (depicted by dash-line box) in the insert shows the structural relaxation of the amorphous state**
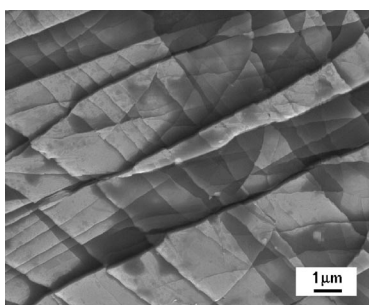
Fig. 2. **The typical morphology of shear bands of the amorphous alloy after repeated impactions**

sample part corresponding to the shear band volume is enhanced with free volume due to the intensive local heating in adiabatic conditions during shear band creation[1].

DSC traces for samples in the state after different plastic deformation as well as in the initial state after annealing are in Fig. 3. All samples exhibit very similar thermal behaviour. The enthalpy change for the as-quenched sample is added for comparison. During annealing at 200 °C for 2 h the sample underwent the structural relaxation and the wide region of enthalpy changes due to free volume annihilation diminished as can be seen on the DSC trace of the annealed sample.

DSC traces of the deformed samples revealed the annihilation of the free volume introduced by plastic deformation. With the increasing the amount of stored deformation energy the larger enthalpy changes are observed. Similar results were obtained in[5,6]. In more deformed sample the amount of shear band regions is higher and so the total free volume increases. In disordered systems the free volume is distributed with activation energy spectrum and therefore the relaxation peak is very wide. At lower temperatures the defects (or free volume) with lower activation energy annihilate[7]. The defects in the as-quenched state begin to anihilate at temperatures above 140 °C. The
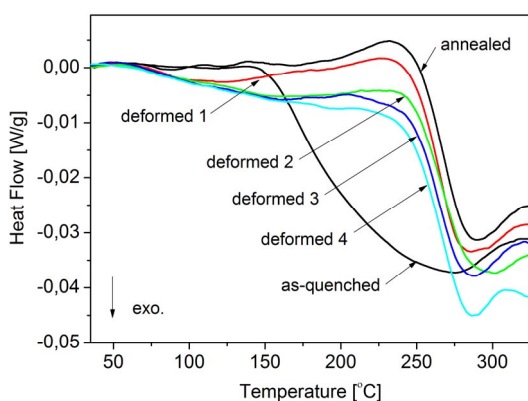
defects introduced by the local plastic deformation have lower activation energy and annihilate at lower temperatures. Moreover, higher deformation causes the increasing the amount of defects with higher activation energy and the deformation is then accumulated into the existing shear bands.

Structural changes in the Fe-Ni-B amorphous ribbon at nanoscale level in the narrow shear bands were studied by means of measuring of integral properties like enthalpy changes. Although the plastic deformation is accumulated into 20 nm-narrow shear bands and the part of the sample volume corresponding to the shear band regions is small, the thermal effects connected with the free volume releasing are observable by DSC method. In this way the deformation-introduced free volume was estimated as 1/3–1/2 of the free volume introduced by rapid cooling during metallic glass preparation.

REFERENCES

1. Bengus V. Z. et al: Int. J. Rapid Solid. *8*, 21 (1993).
2. Ambriško Ľ., Pešek L., Hlebová S.: Chem. Listy *104*, s287 (2010).
3. Zhang Z., Wu F., He G., Eckert J.: J. Mater. Sci. Technol. *23*, 747 (2007).
4. Yoon K.-S., Lee M., Fleury E., Lee J.-Ch.: Acta Mater. *58*, 5295 (2010).
5. Chen Q., Liu L., Chan K.C.: J. Alloys Comp. *467*, 208 (2009).
6. Pan J., Chen Q., Liu L., Li Y.: Acta Mater. *59*, 5146 (2011).
7. Csach K., Ocelík V., Miškuf J., Bengus V.Z., Duhaj P.: IEEE Trans Magn. *30*, 496 (1994).

A. Juríková, K. Csach, and J. Miškuf (*Institute of Experimental Physics of Slovak Academy of Sciences, Košice*): **Evolution of Structure during Local Plastic Deformation in Fe-Ni-B Metallic Glass**

In metastable amorphous metals the structural relaxation is closely related to the free volume annihilation. In the work we studied the deformation-induced structural changes in the Fe-Ni-B amorphous ribbon. The enthalpy changes connected with structural relaxation of the deformed samples as well as non-deformed samples were measured. With the increasing the amount of stored deformation energy the larger enthalpy changes are observed. The deformation-introduced free volume has lower energy and can achieve ~ 1/3 of the free volume amount introduced by rapid quenching of the melt during metallic glass preparation.

Fig. 3. **DSC scans of the Fe-amorphous ribbon in the as-quenched state, in the state after annealing and in four different deformed states**

TESTING OF NEW COMPOSITE MATERIALS BASED ON FABRIC FROM USED TIRES

LUCIA KNAPČÍKOVÁ[a]**, JOZEF HUSÁR**[a]**, MICHAEL HERZOG**[b]**, and LADISLAV PEŠEK**[c]

[a] *Department of Manufacturing Management, Faculty of Manufacturing Technologies of TU of Košice with a seat in Prešov, Bayerova 1, 080 01 Prešov, Slovak Republic,* [b] *Technical University of Applied Sciences, Bahnhofstraße 1, 15745 Wildau, Germany,* [c] *Department of Materials Science, Faculty of Metallurgy, TU of Košice, Letná 9, 040 01 Košice, Slovak Republic*
knapcikova.lucia@gmail.com

1. Introduction

Composites are materials formed from a mixture of two or more components to produce a material with properties or characteristics superior to those of the individual materials[1,2]. The matrix is a continuous phase material which is usually less stiff and weaker than the reinforcement. It is used to hold the reinforcement together and distribute the load among the reinforcements. Reinforcements in the form of fibers, fabric, whiskers, or particles are embedded in the matrix to produce the composite[3,4]. These properties depend mainly on the polymers phase state, temperature, time, size and direction of external forces[1,4]. The hardness value is an important value to characterize the mechanical properties of the material[5,6]. It is gives an indication of the material resistance against wear, its workability, the heat treatment state, etc. The Shore hardness was determined using standard methods.

2. Material, experiments, results

The investigated composite materials were prepared from recycled components. The matrix was polyvinylbutyral produced by Schirmbeck, Germany, arising from the recycling of car glass. We used the recycled material in the flake´s shape[4], dispersed, spherical, spatially oriented with size of 1–25 mm, Fig. 1.

The fibres were from used tires from passenger cars and trucks, extracted by recycling process (company VODS, Slovakia), then cleaned by separation on vibrating screens, FRITSCH (Germany). Fibres were made of synthetic polymer material, based on polyamide and polyester, Fig. 2, with mean diameter of 30 μm and mean length of 3.55 mm. The properties of investigated materials are presented in Tab. I.
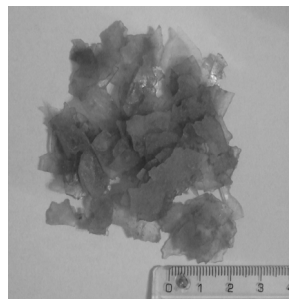

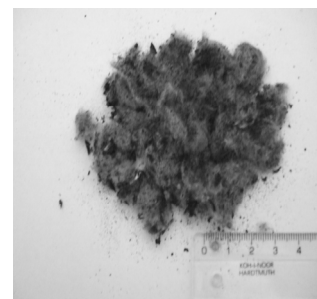Fig. 1. **Recycled polyvinyl-butyral** (Schirmbeck GmbH, Germany)

Fig. 2. **Textiles from used tires** (V.O.D.S., Slovakia)

The homogenization of mixtures was conducted in the temperature range of 80–180 °C (ref.[9]).

The character of the mixing process as well as the emerging nature of the mixture depends on whether the mixed components are completely miscible, partially miscible or completely inmiscible[9,10].

The homogenization began with pre-heating of device at 150 °C, at first adding gradually the thermoplastic material – matrix, polyvinylbutyral, which was thoroughly homogenized for a period of about 30 minutes, then the separated fabrics from used tires were added gradually. On the basis of the previous homogenization of fabrics and PVB, we produced the test boards for 10, 20, 30, 40 and 50 % of fabrics using pressing technology[11,12]. The dependence of tensile strength σ_{max}, Young´s modulus, and tensile strain ε_{max} on percentage ratio of textile in composite materials is presented in Fig. 3. Data were obtained from tensile testing on composite specimens (test board).

Great rubber particles were allways visible on the fracture surface of broken tensile specimens. Young´s

Table I
Mechanical and physical properties of materials

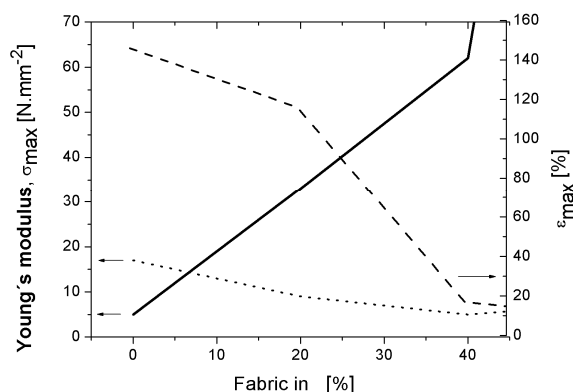| Mechan. and physical properties	PVB Kuraray, GmbH DE[10]	PVB-rec. Schirmbeck GmbH, DE [9]	Fabric from used tires V.O.D.S.,a.s. Slovakia[9]	Kevlar 29 Aramid Fiber DuPont[8]	Comp. material
Young´s modulus [N.mm^{-2}]	3.2	5	-	7.03	5- 62
σ_{max} [N.mm^{-2}]	39.2- 49.2	17.5	-	20.92-3.62	7-18
ε_{max} [%]	205	146	-	3.60	17-146
Shore A/D	70 Shore A	85 Shore A	-	-	36-45 Shore D
T_g [°C]	60-65	50	73	-	46
T_m [°C]	125-200	150	218-255	149-177	259

Fig. 3. **Dependence of tensile strength σ_{max}, tensile strain ε_{max} at tensile strength and Young´s modulus E on % ratio of fabrics** (Young´s modulus ———, σ_{max} . . . . , ε_{max} - - - - -)

Fig. 5. **SHORE hardness for average value of test boards**

modulus of the material increases with increasing the content of textile fibres in the composite material. However, both the tensile strength σ_{max} and tensile strain ε_{max} decrease.

After pressing the test boards, ineligible rubber particles (1–3 mm in the size) were visible in some areas, Fig. 4. The Shore hardness (durometer hardness[6], DIN 53505-D) was analyzed on the composite material with 50 % textile using a Durometer indenter on test boards, 200×200×6 mm (ref.[14]), by 23 °C and 60 % humidity.

Three boards were tested for each composite on that places where appeared broken rubber particles which were part of the textile and materials remained in spite of separation on vibrating screens[7,13]. The hardness measurement began always starting from the centre of rubber particle (distance = 0, Fig. 5), going away up to 15 mm from the edge of the sample. The distance between the individual indents was 5 mm. The analysed area with one Shore hardness indent[5] was about 1 × 1 mm. The ineligible rubber particles which remained after separation play a significant role and affect negatively fracture properties of the composite. The Shore D hardness in the rubber particle (distance
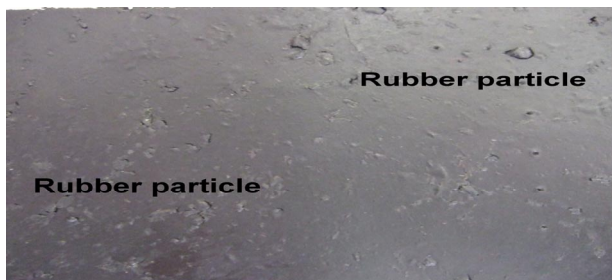
= 0) is higher (41–42), the material around the particles is softer (37–38), Fig. 5.

Conclusions

Based on testing of local and global mechanical properties of composites based on fabric from used tires and recycled polyvinylbutyral can be concluded:

–　Increasing the fabric volume from 0 up to 40 % the Young´s modulus E is linearly increasing from 5 up to 62 MPa, the tensile strength is linearly decreasing from 17 to 7 MPa, the ε_{max} is sharply decreasing from 146 to 17 %.

–　Near the bigger rubber particles was detected an affected zone with lower hardness, which was the cause of fracture.

REFERENCES

1. Eichlerová R. et al.: Chem. Listy *104*, s307 (2010).
2. Zamfirova G. et al.: Chem. Listy *104*, s283 (2010).
3. Vasiliev V. V., Morozov V. E.: *Mechanics and Analysis of Composite Materials*, Elsevier 2001.
4. Nielsen E. L., Landel F. R.: *Mechanics and Analysis of Composite Materials*, Elsevier 2001.
5. Vable M.: Mechanics of materials, Available on internet : <www.me.mtu.edu>, download 20.6.2011.
6. Zaťko M., Eckhardt E.: Methods for measuring of materials hardness and principles by choosing portable devices for measuring, Available on internet : <www. ssndt.sk >, download 20.6. 2011
7. Shore (Durometer) Hardness Testing of Plastics, Available on internet : <www.matweb.com/reference/shore-hardness.aspx> download 17.5.2011.
8. DuPont, Product Kevlar 29Aramid Fiber, Available on internet: <www. matweb.com>, download 10.9.2011.

Fig. 4. **Composite material with ineligible rubber particles**

9. Knapčíková L., Herzog M., Oravec P.: Manuf. Eng. Vol. *4* (2010).
10. Kuraray, Product Mowital B 30 T, Available on internet : <www. kuraray.com>, download10.9.2011.
11. Schuermann H.:*Konstruktieren mit Faser-Kunststoff Verbunden*, Springer Berlin 2001.
12. Švorčík V.: *Structure and Properties of Polymers*, VŠCHT, Praha 2010.
13. Zubko P. et al.: Chem. Listy *104*, s390 (2010).
14. DIN- Taschenbuch*, Kunststoffe- Mechanische und thermomechanische Eigenschaften*, Beuth 1997.

L. Knapčíková[a], J. Husár[a], M. Herzog[b], and L. Pešek[c] *([a]Department of Manufacturing Management, Faculty of Manufacturing Technologies of TU of Košice, [b]TU of Applied Sciences, Wildau, Germany, [c]Department of Materials Science, Faculty of Metallurgy, TU of Košice, Slovak Republic):* **Testing of New Composite Materials Based on Fabric from Used Tires**

The paper deals with testing of new composite materials based on fabric from used tires. The matrix in the composite material is a thermoplastic polyvinylbutyral (PVB), which was obtained after recycling the carglass, where it forms a part of the safety film. The goal of this paper is to present the analysis of mechanical properties of composite materials with various (10–40 %) volume fraction of fabric. Ineligible rubber particles (1–3 mm) were detected in some areas which are remained after separation, they play a significant and detrimental role and affect the mechanical properties of the composite.

PRODUCTION AND TESTING OF THERMOCOUPLES TYPE Cu-CuNi

LADISLAV KOLAŘÍK[a], MARIE VÁLOVÁ[a], PETR VONDROUŠ[a], KAREL KOVANDA[a], and JOSEF ŠEPITKA[b]

[a] *Department of Manufacturing Technology, Faculty of Mechanical Engineering, Czech Technical University, Technická 4, 166 07 Praha 6, Czech Republic,* [b] *Czech Technical University in Prague, Faculty of Mechanical Engineering, Dept. of Mechanics, Biomechanics and Mechatronics, Technicka 4, 166 07 Prague, Czech Republic* ladislav.kolarik@fs.cvut.cz

1. Introduction

Purpose of special fast thermocouples is to measure temperature of fast thermal processes with very little time delay (few ms). The response of the thermocouple to the real temperature of the environment depends mainly on heat capacity of the thermocouple and it´s encapsulation. To fasten the response of measurement no encapsulation and the thinnest wire should be used. But such a thermocouple would be damaged in the measurement, so it is only for single usage.

Such a thin thermocouples, with wires of diameter in the scale of 1–100 μm, can be used to measure the real temperatures of the combustion products of explosives, propellants and so on. Interesting application includes temperature measurement of combustion products during airbag ignition in the car[1].

Because the thermocouple needs to have both wires welded, main difficulty producing thin thermocouples is the welding technology giving high quality welds with perfect repeatability of the welding process and results.

2. Experimental

As welding technology we have selected microplasma welding (micro-PAW), because it offers advatages for welding of thin materials (e.g. thermocouples). Plasma arc has very high temperature (up to 25 000 °C), has high energy density, is very stable and well controlable. All these features improve possibility to create sound welds even on very thin materials and wires. Plasma Arc Welding (PAW) has developed from Gas Tungsten Arc Welding (GTAW). In PAW the arc is struck between tungsten electrode and Cu nozzle. By the flow of the plasma gas

through the copper nozzle the created plasma is forced to exit the orifice of the nozzle and becomes the heat source, which is very stable and well controlable by setting the current and plasma gas flow. The schematic of the micro-PAW welding method is at the Fig. 1.

For the construction of thermocouples copper, nickel, chromium, platinum alloys are used. Often used thermocouples are e.g. Cu-CuNi, Fe-CuNi, NiCr-Ni, Pt-PtRh. As the basic thermocouple for testing suitability of micro-PAW for welding of thermocouples the Cu-CuNi thermocouple was selected because easy availability of Cu and CuNi (konstantan) wire at the market. Cu-CuNi thermocouple can be used easily in the temperature range from –250 to +400 °C where it´s temperature resistivity is linear.

Cu and CuNi wires, both of diameter 0.1 mm, were used and welded by micro-PAW with very low welding parameters. Set welding current was $I = 5$ A. Tungsten-thorium electrode (WT) with diameter 1 mm and transferred arc wiring was used. At the Fig. 1 the transferred arc can is done by connecting the switch at the position 11.

Weld quality and fusion of the 2 metals was checked by metallography. Because of the miniature size of the sample the metallography was rather difficult. Special fixing of the sample in the thermoset with very low thermal shrinkage, grinding with SiC emery paper 2500, 4000, polishing with diamond (3 μm) and coloid silica was necessary. For etching (1 part HNO_3 and 9 parts H_2O) was used and photographs are done on metallurgical microscope (Carl Zeiss – AxioObserver D1m) in DIC contrast. Microhardness according to Vickers (load 10 g) of the
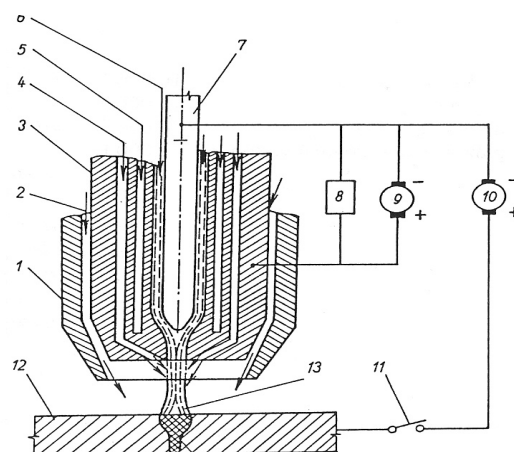

Fig. 1. **Scheme of micro plasma arc welding,** 1 – shielding nozzle, 2 – shielding gas, 3 – water cooled nozzle, tube, nozzle, 4 – focusing gas, 5 – water cooling, 6 – plasma gas, 7 – tungsten electrode, 8 – high frequency ionizator, 9,10 – power source, 11 – switch, 12 – BM, 13 – plasma arc

base metals (wires) and across the joint was measured along the red dashed line shown on Fig. 2. By Hysitron system the nanohardness and Young´s modulus of the BM and WM were measured (load of 1 mN). This measurement was done acoording to Oliver and Pharr[2] using Berkovich indeter, because it is very favourable for small samples (diameter 0.1 mm).

3. Results and discussion

The heterogeneous joint of welded Cu-CuNi thermocouple had a favorable circular shape.

The metallographic cut of the welded thermocouple was done to check penetration, size and quality of joint. The cut is shown at the Fig. 2, where the regular circular shape is visible.

The average results of nanohardness measurement and Young modulus is stated in Table I.

At the Fig. 3 is shown measurement of the Vickers hardness along the red dashed line drawn at the Fig. 2. It is obvious that the joint is ductile without any hard brittle phases, because hardness in HAZ and WM the hardness is quite low, approx. between 70–200 HV0.01, without any hardness peaks.

Hardness measurement by nanoindentation was done. Nanoindentation was made in different parts of the welded part – see Fig. 4. Both measured results are in reciprocal compliance.

Fig. 2. **Welded thermocouple Cu-CuNi, upper wire - Cu, lower wire - CuNi**

Table I
Average values of Young´s modulus and nanohardness

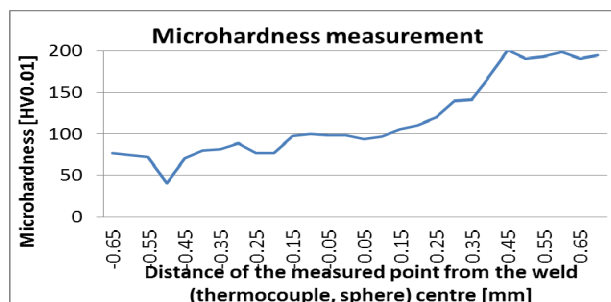| Material	E_{IT} [GPa]	H_{IT} [GPa]
Cu	119.9 ± 5.5	2.29 ± 0.07
CuNi	153.6 ± 6.0	3.43 ± 0.28
weld	148.9 ± 3.8	2.71 ± 0.06

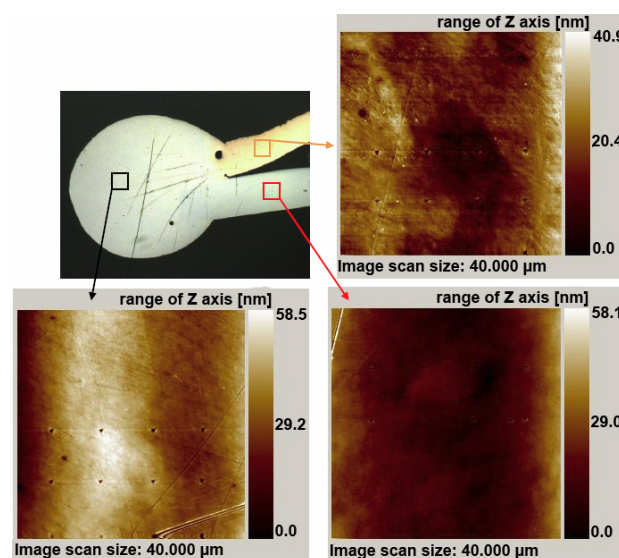Fig. 3. **Microhardness of the welded thermocouple**

Fig. 4. **Areas of welded sample nano indentation measurement, tested area 40×40 μm, measured results stated in Table I**

4. Conclusion

The creation of the thermocouple Cu-CuNi with favorable circular shape of the weld joint was possible by microplasma welding. No hard brittle phases were found by hardness measurement, so mechanical strength of the joint is satisfactory without any risk of brittle failure. It is possible to say that technology suitable for welding of heterogeneous joints of thin Cu-CuNi thermocouples was found.

REFERENCES
1. Lengellé G., Duterque J., Trubert J. F.: RTO-EN-023, Belgium 2002.
2. Oliver W. C., Pharr G. M.: J. Mater. Res. *7*, 1564 (1992).

L. Kolařík[a], M. Válová[a], P. Vondrouš[a], K. Kovanda[a], and J. Šepitka[b] (*[a] Dept. of Man. Tech., [b] Dept. of Biomechanics, Faculty of Mech. Eng., CTU in Prague, Prague, Czech Republic)* **Production and Testing of Thermocouples Type Cu-CuNi**

This article focuses on production and testing of thermocouples. Thermocouples Cu-CuNi with fast response for measurement of real thermal cycles during explosions were welded. This work includes details of welding technology and results of testing of the weld by metallography, microhardness and also Hysitron nanoindentation measurement.

TESTING OF DUPLEX COATINGS BY MODULUS MAPPING METHOD

MARIE KOLAŘÍKOVÁ
and JAN SUCHÁNEK

Department of Manufacturing Technology, Faculty of Mechanical Engineering, CTU in Prague, Technická, 166 07 Prague, Czech Republic
marie.valova@fs.cvut.cz

1. Introduction

This paper presents results of tribological testing of duplex coatings that have been presented in the previously published paper "The Effect of Duplex Coating on Wear Properties of Tool Steels"[1]. In detail it includes results of testing by Modulus Mapping[TM] method. Modulus Mapping combines *in-situ* SPM imaging capability of Hysitron's nanomechanical testing instruments with the ability to perform dynamic, or nanoDMA tests.

2. Experiment

The specimens from the low-alloy steel 31CrMoV9 were inert gas quenched and tempered. The duplex treatment had two phases. In the first phase, the specimens were pulse plasma nitrided (depth of nitrided layer is 70 μm). In the second phase, various PVD coatings were deposited: TiN, CrN, TiAlN and a multilayer 3×(TiN-CrN). All coatings were 3 μm thick. Because of the miniature size of the coating, the metallography was rather difficult. There were also problems with the production of sample because plannar surface was required for measurement. The difference in hardness of the substrate, PVD coating and mounting materials cause grinding of sample edge. Therefore, a small steel plate with the same hardness as the base material sample was glued on the coatings. Then the edge gringing was minimalized and the plannarity of the sample was sufficient for nanomechanical tests.

Special mounting of the specimens in thermoset with very low thermal shrinkage, grinding with SiC emery paper with 2500 and 4000 grit and polishing with diamond (3 μm) and coloid silica were necessary. Photographs were taken in a metallurgical microscope (Carl Zeiss – AxioObserver D1m). Treated specimens were tested on Hysitron TI 950 TriboIndenter™ to obtain 3D topography of cross section and a map of complex modulus. The measurement methods are described in details in ref.[1] and ref.[2].

The analysis of the dynamic test is derived from the classical equation for a single degree of freedom harmonic oscillator as given in Eq. (*1*):

$$F_o \sin(\omega t) = mx'' + Cx' + kx \qquad (1)$$

where F_o is the magnitude of the sinusoidal force, ω is the frequency of the applied force, m is the mass, C is the damping coefficient and k is the stiffness of the system. The solution to this differential equation is seen as Eq. (*2*) where a displacement amplitude response (denoted as X_o) is given for a given sinusoidal force F_o, at a frequency ω for a system with a given stiffness, mass and damping.

$$X_o = \frac{F_o}{\sqrt{(k - m\omega^2)^2 + ((C_i + C_s)\omega)^2}} \qquad (2)$$

The phase difference between the force and the displacement is given in Eq. (*3*):

$$\phi = \tan^{-1}\frac{(C_i + C_s)\omega}{k - m\omega^2} \qquad (3)$$

where the total spring stiffness, k, consists of two parts,

$$k = k_s + k_i \qquad (4)$$

The subscripts in Eq. (*1–4*), i and s stand for indenter and sample respectively. From a dynamic calibration m, C_i, and K_i are known, X_o and $ø$ are measured, leaving K_s and C_s as the only unknown variables. By assuming a linear viscoelastic response, these equations can be used to calculate the stiffness and damping of a system from the displacement amplitude and phase lag. The stiffness and damping can be used for calculation of the storage modulus and loss modulus using Eq. *5*a and b.

$$E' = \frac{k_s \sqrt{\pi}}{2\sqrt{A_c}} \qquad E'' = \frac{\omega C_s \sqrt{\pi}}{2\sqrt{A_c}} \qquad a = \left(\frac{3FR}{4E_r'}\right)^{\frac{1}{3}} \qquad (5)$$
a)   b)   c)

where a is the radius of the contact area and R is the radius of curvature of the tip[5].

Eq. (*6*) shows the relationship between complex modulus (denoted as $E*$), storage modulus (denoted as E'), and loss modulus (denoted as E''), where i is the imaginary unit.

$$E* = E' + iE'' \qquad (6)$$

Another theory is presented in ref.[4] and ref[5].

3. Results

Results of Modulus Mapping are shown in Fig. 1 and Fig. 2. Topographic information obtained by *in-situ* SPM is shown in Fig. 3. The tested area was 5×5 μm. We can
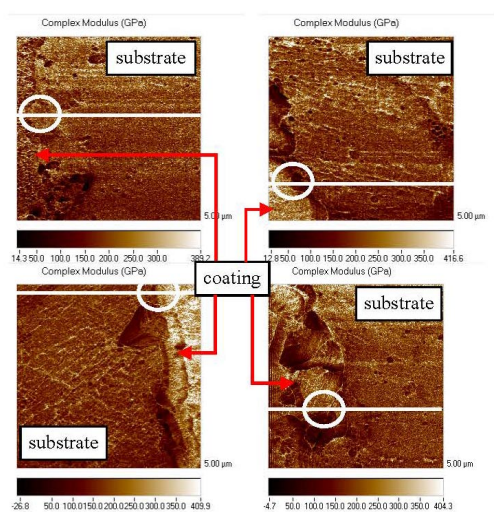
Fig. 1. **Maps of complex modulus for individual coatings: CrN (top left), TiN (top right), TiAlN (bottom left) and multilayer 3×(TiN-CrN) (bottom right). The area in red circle represents a transition zone between substrate and PVD layer**
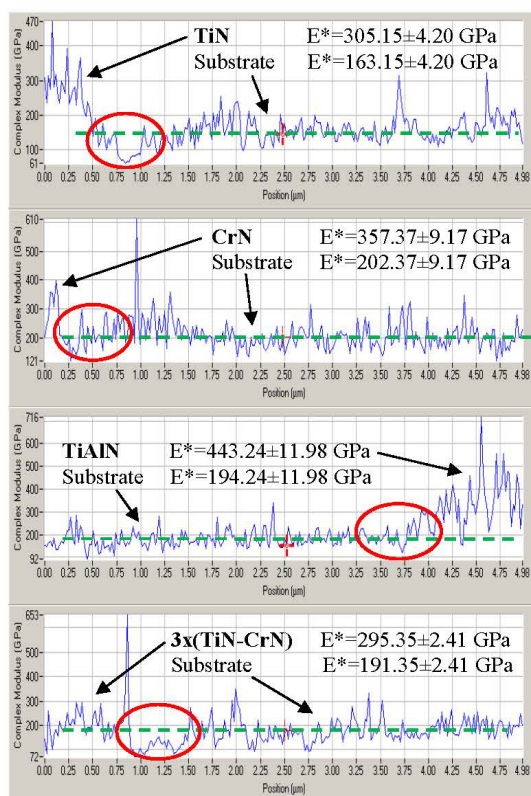

Fig. 2. **Analyses of complex modulus on cross section (The area in red circle represents a transition zone between substrate and PVD layer. The green dashed line shows the average value of complex modulus of substrate)**
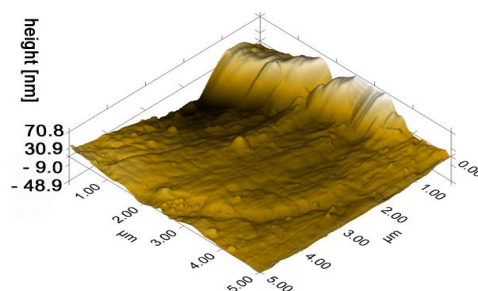

Fig. 3. **Example of topographic information for individual coatings obtained by *in-situ* SPM**

see an increase in values of complex modulus on the area of PVD coating. Measured values of complex modulus are CrN ~ 357 GPa, TiN ~ 305 GPa, TiAlN ~ 443 GPa and 3× (TiN-CrN) ~ 295 GPa.

Complete results of tribological tests are given in ref.[2] and ref.[3].

4. Conclusion

Results for all coatings show that deposited PVD coatings did not affect the properties of nitrided base material. No gradient or transition layer between deposited coating and substrate were observed.

REFERENCES

1. Válová M., Suchánek J.: Chem. Listy *105*, s856 (2011).
2. Lukeš J., Šepitka J., Němeček J.: Chem. Listy *104*, s338 (2010).
3. Válová M., Suchánek J., Bláhová O.: Chem. Listy *104*, s378 (2010).
4. Asif S., Wahl K., Warren O.: J. Appl. Phys. *90*, 1192 (2001).
5. Sepitka J., Lukes J., Kuzelka J., Rezníček J.: Chem. Listy *105*, s844 (2011).

M. Kolaříková, and J. Suchánek *(CTU in Prague, Prague, Czech Republic):* **Testing of Duplex Coatings by Modulus Mapping Method**

The paper summarizes partial results of tribological testing of tool steels with duplex coating. Steel samples (31CrMoV9) were nitrided and subsequently treated by PVD process. Different types of coatings (TiN, CrN, TiAlN and a multilayer 3×(CrN-TiN)) with a thickness 3 μm were deposited on samples. The following properties were measured: Results of Modulus Mapping^{TM} are summarized in this paper.

TWO-SCALE MODEL FOR PREDICTION OF MACROSCOPIC ELASTIC PROPERTIES OF ALUMINIUM FOAM

VLASTIMIL KRÁLÍK and JIŘÍ NĚMEČEK

Czech Technical University in Prague, Thákurova 7, 166 29 Prague 6, Czech Republic
vlastimil.kralik@fsv.cvut.cz

Keywords: metal foam, porous system, nanoindentation, micromechanical properties, homogenization

1. Introduction

Aluminium foams belong to the group of modern structural materials with high potential to many engineering applications. It is a highly porous material with cellular inner microstructure. It is also known for attractive mechanical and physical properties. The application of this material is very wide. Some structural and functional applications of aluminium foams for industrial sector which covers mainly automotive, aircraft but also building industries have been reviewed e.g. by Banhart[1].

In this study, commercially available aluminium foam Alporas® (Shinko Wire Co., Ltd) was tested. Alporas is characterized by a closed cell microstructure as shown in Fig. 2. The large inner pores have usually round of polyhedral shape with the mean size ~ 4.5 mm[2]. The very thin cell walls (typically ~ 100 μm thick, Fig. 1) of closed cells create randomly distributed solid metal phase. The overall porosity of this material reaches ~ 90 % (ref.[2]). The manufacturing process of the Alporas is a batch casting process and can be found in details e.g. in Miyoshi et. al.[2].

In this paper, we deal with the assessment of the two-scale microstructural model that takes into account heterogeneity taking place on the cell wall level, as well as at the whole foam level. For this reason, we utilize micromechanical up-scaling procedures that are commonly used in finding effective properties of classical composites. Up-scaling mechanical properties from microscale to the upper level uses so called homogenization techniques[3] in which microscopically heterogeneous material is replaced by a fictitious homogeneous one having equivalent overall behavior.

2. Definition of the model

The Alporas foam is characterized by a hierarchical microstructure. At least two characteristic length scales can be distinguished: the cell wall level and the foam level. Therefore, two-scale microstructural model for the prediction of macroscopic elastic properties on the whole foam level is proposed based on the utilization of nanoindentation data received on cell walls[4]. The model covers:

Level I (the cell wall level).

In this level, characteristic dimension of the cell wall defined by the mean midspan wall thickness is $L \sim 100$ μm. This level consists of prevailing aluminium matrix (Al-rich area) with embedded heterogeneities in the form of Ca/Ti-rich areas (as further discussed in section 3.2). Distinct elastic properties of the microstructural constituents were assesed using nanoindentation at this level.

Level II (the foam level).

At this level, the whole foam containing large pores with an average diameter ~ 2.6 mm (as evaluated for our samples) are considered. Cell walls are considered as homogeneous having the properties that come from the Level I homogenization.
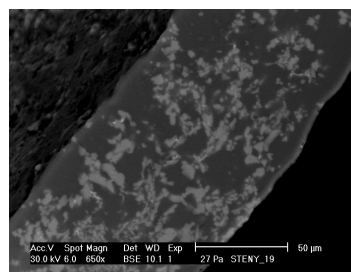
Fig. 1. **Detailed ESEM image of a cell wall showing Ca/Ti-rich area (light zones) – Level I**
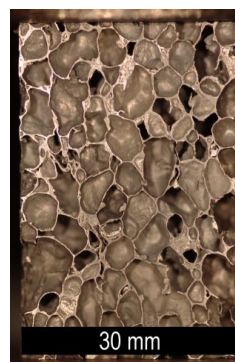

Fig. 2. **Overall view on a typical micostructure of aluminium foam – Level II**

3. Experimental part

3.1. Sample preparation

Samples for nanoindentation testing were prepared from small Alporas block 18×18×14 mm which was firstly embedded into cylindrical mould and filled with a low viscosity epoxy resin (Struers®). Then, ~ 5 mm slice was cut

by diamond saw and polished with fine SiC papers with selected technological process[5]. Resulting surface roughness was checked with *in-situ* imaging (surface scanning was performed with the same tip as for nanoindentation). Quadratic deviation from the mean plane (root-mean-square[6]) was found to be $R_q \approx 9$ nm which was more than acceptable compared to the maximum indentation depths 100–300 nm. As a rule of thumb, the surface roughness should be kept within 10 % of the expected maximum depths used in nanoindentation which was fullfilled in our case.

3.2. ESEM and microstructural analysis

The microstructure of the cell wall was studied in electron microscope (ESEM). Two distinct phases, visible as differently colored areas in ESEM images were identified (Fig. 1). The chemical composition of the two phases was checked with EDX element analysis in ESEM. As expected, the majority of the volume (dark zone) was composed of aluminum and aluminium oxide Al_2O_3 (further denoted as Al-rich area). Lighter zones contained significant amount of calcium and titanium (further denoted as Ca/Ti-rich area). The non-uniform distribution of these zones shows on inhomogeneous mixing of the admixtures added during the production process.

3.3. Nanoindentation

The nanoindentation testing was performed using a Hysitron Tribolab system® located at the CTU Prague's laboratory. This system consists of *in-situ* SPM imaging which was used for scanning the sample surface. Berkovich tip was used for all measurements.

Two distant locations were chosen on the sample to capture its heterogeneity. Both locationss were covered by a grid of 10×10 indents with 10 μm spacing. It yields 200 indents in total which was considered to give sufficiently large statistical set of data. Standard load controlled test for an individual indent consisted of three segments: loading, holding at the peak and unloading. Loading and unloading of this trapezoidal loading function lasted for 5 s, the holding part lasted for 10 s. Maximum applied load was 1500 μN.

3.4. Results of the experimental part

Elastic modulus was evaluated for individual indents using standard Oliver and Pharr methodology[7]. The results are depicted in Fig. 3 in which a frequency plot of all elastic moduli merged from two different positions are shown. No significant differences between the positions were found.

Statistical results of elastic moduli have been further analyzed with a deconvolution technique[8–10] which seeks for parameters of individual phases covered in overall results. The deconvolution algorithm searches for n-Gauss distributions in an experimental probability density func-

tion (Fig. 3). Random seed and minimizing criteria of the differences between the experimental and theoretical overall PDFs are computed in the algorithm to find the best fit[9]. Two-phase system (one dominant Al-rich phase and one minor Ca/Ti-rich phase) was assumed in the deconvolution. Tab. I contains numerical results from the deconvolution with the estimated volume fractions of the phases.

It can be seen in Fig. 3 that a significant peak appears around 62 GPa appears. This value can be considered as a dominant characteristic of the Al-rich solid phase. This value is in excellent agreement with the value measured by Jeon et al.[11] on melted Al-1.5 wt.% Ca alloy (61.7 GPa).
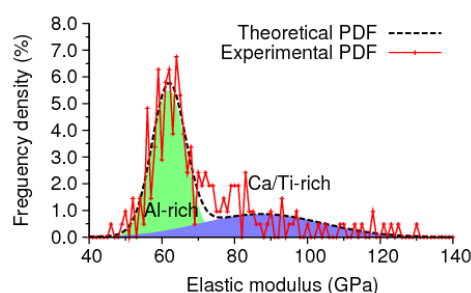

Fig. 3. **Deconvolution of elastic moduli in two phases (Al-rich and Ca/Ti-rich) from two measured positions**

Table I
Elastic moduli and volume fractions from deconvolution

Phase	Mean [GPa]	St. dev. [GPa]	Volume fraction
1 (Al-rich zone)	61.9	4.6	0.638
2 (Ca/Ti-rich zone)	87	17	0.362

4. Numerical part

4.1. Level I homogenization

Continuum micromechanics provides a framework, in which elastic properties of heterogeneous microscale phases are homogenized to give overall effective properties on the upper scale[3]. A significant group of analytical homogenization methods relies on the Eshelby's solution[12] that uses an assumption of the uniform stress field in an ellipsoidal inclusion emnedded in an infinite body. Effective elastic properties are then obtained through averaging over the local contributions[3]. Based on previous experience, we selected two most frequently used analytical schemes and two bounds in the following. At first, rough estimates can be done by computing bounds (limits) based on mixture laws of Voight (parallel configuration of phases with perfect bonding) and Reuss (serial configura-

tion of phases). The disadvantage of using these bounds (or limits) is that they are usually quite far from each other.

Very often, the Mori-Tanaka method[8] can be used for the homogenization of composites with continuous matrix reinforced with discontinuous spherical inclusions. In this method, the effective bulk k_{eff} and shear μ_{eff} moduli of the composite are computed as follows:

$$k_{eff} = \frac{\sum_r f_r k_r (1 + \alpha_0 (\frac{k_r}{k_0} - 1))^{-1}}{\sum_r f_r (1 + \alpha_0 (\frac{k_r}{k_0} - 1))^{-1}} \quad (1)$$

$$\mu_{eff} = \frac{\sum_r f_r \mu_r (1 + \beta_0 (\frac{\mu_r}{\mu_0} - 1))^{-1}}{\sum_r f_r (1 + \beta_0 (\frac{\mu_r}{\mu_0} - 1))^{-1}} \quad (2)$$

$$\alpha_0 = \frac{3k_0}{3k_0 + 4\mu_0}, \beta_0 = \frac{6k_0 + 12\mu_0}{15k_0 + 20\mu_0} \quad (3)$$

where f_r is the volume fraction of the rth phase, k_r its bulk modulus and the coefficients α_0 and β_0 describe bulk and shear properties of the 0th phase, i.e. the reference medium[3]. The bulk and shear moduli can be directly linked with Young's modulus E and Poisson's ratio v used in engineering computations as:

$$E = \frac{9k\mu}{3k + \mu} \quad (4)$$

$$v = \frac{3k - 2\mu}{6k + 2\mu} \quad (5)$$

At second, the self-consistent scheme[3] was used. It is an implicit scheme, similar to Mori-Tanaka method, in which the reference medium points back to the homogenized medium itself.

The homogenized elastic property for the two considered microscale phases in the cell wall (i.e. Level I) is summarized in Tab. II for individual homogenization techniques. Very close bounds and insignificant differencies in the elastic moduli estimated by the schemes were found.

4.2. Level II homogenization

In this level, cell walls are considered as a homogeneous phase having the properties that come from the Level I homogenization. The walls createa matrix phase and the large air pores can be considered as inclusions in this homogenization.

At first, effective elastic properties of the Level II were estimated with the same analytical schemes used in Level I. The volume of air pores was assessed experimentally by weighing on our samples as 91.4 %. The homogenized elastic modulus for the Level II structure is summarized in Tab. III. It is clear that the analytical methods do not give appropriate results, because the basic assumptions following from Eshelby's solution of an ellipsoidal inclusion in an infinite body and volume fraction restrictions are not fulfilled. Nevertheless, the correct solution should lie between Voight and Reuss bounds that are, in this case, quite distant (Tab. III). The Mori-Tanaka ends up close to the average phase value, whereas the self-consistent scheme tends to reach lower stiffness value (i.e. the air) due to the very large volume fraction of pores.

At second, more appropriate two dimensional microstructural FEM model was applied. The model geometry was generated from high resolution optical images of Al-foam cross-section (Fig. 4a), which was embedded to blackwashed gypsum and than polished with fine SiC papers. Size of this representative area is 36 × 44 mm and represents a higher structural level of the material. At this image, pore centroids were detected, Delaunay triangulation applied and Voronoi cells created. Then, an equivalent 2D-beam structure was generated from cell boundaries (Fig. 4b). As a first estimate, uniform cross-sectional area was prescribed to all beams (~ 8.6 % of the total). Boundary conditions appropriate to the loading (axial tension) are specified in Fig. 4b. The tension test leading to the evaluation of the homogenized elastic modulus was performed using program Oofem software package[13].

In our computations, the homogenized elastic modulus reached $E_{hom} \approx 0.3-0.6$ GPa depending on the stiffness of the contour beams. The higher E_{hom} value appllies for the contour beam stiffness which has the same stiffness as the rest of the beams. The lower E_{hom} value applies if a half

Table II
Effective values of Young's modulus computed by different homogenization schemes

Scheme	Mori-Tanaka	Self-consist. scheme	Voigt bound	Reuss bound
E [GPa]	70.076	70.135	71.118	69.195

Table III
Effective values of Young's modulus by different homogenization schemes

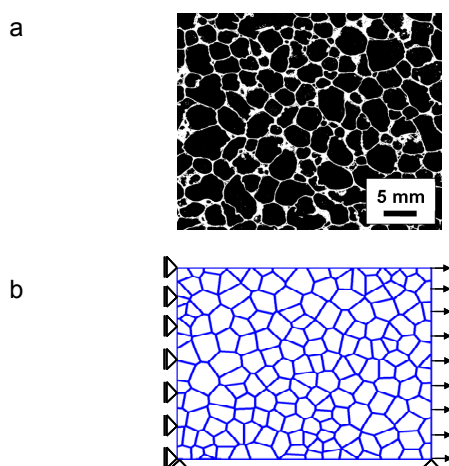| Scheme	Mori-Tanaka	Self-consist. scheme	Voigt bound	Reuss bound
E [GPa]	3.1510	0.0012	6.0200	0.0011

a

b

Fig. 4. **(a) High resolution optical image of Al-foam. (b) 2D-beam structure with prescribed boundary conditions**

-stiffness is used for contour beams. Such result is in good agreement with the range of experimental values (0.4−1 GPa) reported for Alporas® e.g. by Ashby et. al.[14]. Our preliminary experiments show on the E_{hom} value 0.27 GPa.

5. Conclusions

Elastic parameters of cell walls were obtained on a statistical set of nanoindentation results from which one dominant and one minor mechanical phase were separated by the deconvolution algorithm. Analytical homogenization schemes showed very similar results of effective cell wall elastic properties ($E_{Level-I} \approx 70$ GPa). This value together with corresponding volume fraction of cell walls and large pores were used in micromechanical up-scaling to the upper level (Level II). Effective elastic properties of Level II were estimated with the same analytical schemes used in Level I. However, the analytical methods do not give satisfactory results in this case. Therefore more appropriate two dimensional microstructural FEM model was applied. Homogenized elastic modulus reached 0.3−0.6 GPa. These values are in good agreement with the range of experimental values obtained by conventional methods. Further development of the numerical model (influence of boudary conditions, influence of beam stiffness variations, size of RVE, extension to 3D) and extending an experimental program is planned in the future.

REFERENCES

1. Banhart J.: Prog. Mater. Sci. *46*, 559 (2001).
2. Miyoshi T., Itoh M., Akiyama S., Kitahara A.: Mater. Res. Soc. Symp. Proc. *521*, 133 (1998).
3. Zaoui A.: J. Eng. Mechanics *128*, 808 (2002).
4. Němeček J., Králík V., Vondřejc J., Němečková J.: *Proceedings of the Thirteenth International Conference on Civil, Structural and Environmental Engineering Computing*. Edinburgh: Civil-Comp Press (2011).
5. Dudíková M., Kytýř D., Doktor T., Jiroušek O.: Chem. Listy *105*, s790(2010).
6. ISO 4287-1997, "Geometrical Product Specifications (GPS) − Surface texture: Profile method − Terms, definitions and surface texture parameters".
7. Oliver W., Pharr G. M.: J. Mater. Res. *7*, 1564 (1992).
8. Constantinides G., Chandran K. R., Ulm F.-J., Vliet K. V.: Mater. Sci. Eng., A *430*, 189 (2006).
9. Němeček J., Šmilauer V., Kopecký L.: Cem. Concr. Composites *33*, 2 (2011).
10. Tesárek P., Němeček J.: Chem. Listy *105*, 17 (2010).
11. Jeon I. et al.: Mechanics Mater. *41*, 60 (2009).
12. Eshelby J. D.: Proc. Royal Society *241*, 376 (1957).
13. Patzák B., Bittnar Z.: Adv. Eng. Software *32*, 759 (2001).
14. Ashby M. F., Evans A., Fleck N. A., Gibson L. J., Hutchinson J. W., Wadley H. N.: Mater. Design *23*, 1 (2002).

V. Králík and J. Němeček *(Czech Technical University in Prague, Faculty of Civil Engineering):* **Two-scale Model for Prediction of Macroscopic Elastic Properties of Aluminium Foam**

This paper is focused on the prediction of macroscopic elastic properties of highly porous aluminium foam. The material is characterized by a closed pore system with very thin pore walls and large air pores. Intrinsic material properties of cell wall constituents are assessed with nanoindentation whereas analytical homogenizations are employed for the assessment of the cell wall elastic properties. 2D microstructural FEM model was applied to obtain effective elastic properties of the whole foam.

SIZE-DEPENDENT MICROHARDNESS OF TWO-COMPONENT SINTERED MATERIALS

MIRIAM KUPKOVÁ[a] and MARTIN KUPKA[b]

[a] *Institute of Materials Research of SAS, Watsonova 47, Košice,* [b] *Institute of Experimental Physics of SAS, Watsonova 47, Košice, Slovakia*
mkupkova@imr.saske.sk

1. Introduction

Indentation techniques are widely used in the industry for more than one century. They serve as quality control measurements and as an economical, routine probe for estimating the strength of engineering materials. Indentation tests offer simplicity and speed because they require access only to a flat surface of component rather than, for example, the manufacturing of special specimen for conventional tensile testing. In connection with microdevices, material scientists discovered that they could quickly and conveniently probe the small-scale response of material dimensions by micro- and nanoindentation techniques.

In the Brinell test, a hard ball of diameter D is pressed under a load P into the plane surface to be examined. After removal of the load, the chordal diameter d of a remanent impression left by the indenter is measured. The Meyer hardness H_M is calculated as the load divided by the projected area of the impression.

Tabor[1] demonstrated that for metals with a power-law work-hardening the Meyer hardness is

$$H_M \equiv \frac{4P}{\pi d^2} \approx 3Y_0 \left(0.2 \frac{d}{D} \right)^n , \qquad (1)$$

and the plot Meyer hardness versus d/D closely reproduces the tensile true stress versus true strain curve. Here Y_0 is a critical tensile stress below which the deformation is elastic, and n is work hardening exponent.

So, by making a series of Brinell tests with indentations of various diameter d the important plastic stress-strain characteristics of the material may be extracted from the observed H_M-d relation.

As regards the conical or pyramidal indenters, Tabor argued that due to the "principle of geometric similarity" the hardness should not depend on the size of the remanent impression left by the indenter or on the indentation load. He demonstrated that for the Vickers indenter

$$H_M \equiv \frac{2P}{d^2} \approx 3(Y \text{ at } 8\% \text{ strain}). \qquad (2)$$

Here d represents the Vickers indent diagonal.

Conical or pyramidal indenters whose sizes exceed tens of microns really produce size-independent hardness values for most metals.

But smaller indenters, in the range from submicrons to about ten microns, often display a significant size effect. That is, the impressions left by such indenters are smaller than expected from the size of impressions left by large indenters. Thus the apparent hardness of a specimen increases as the impression size decreases.

The increase in strength is explained in terms of the local dislocation hardening due to geometrically necessary dislocations (GNDs). These dislocations are required to account for the permanent shape change at the surface. The micron-scale permanent impressions produce the densities of GNDs that are comparable to or exceed the densities of statistically stored dislocations, that is the dislocations present in the material prior to the indentation. The smaller is the size of the non-uniform deformation, the larger is the relative density of the GNDs and the greater is their contribution to the work hardening.

This explanation is suitable for behaviour after plastic deformation has started and the indentation process is "well developed". This theory cannot describe the situation near the initial deviation from the elastic regime at the initiation of the plasticity, as there are no GNDs. So, the hardness data may not follow the theory for very small impression sizes.

2. Theory

The objective of this contribution is to modify the Nix and Gao model to account for the indentation of solid solutions.

Nix and Gao[2] considered the indentation of a pure metal by a rigid cone. Resultant impression is accommodated by circular loops of GNDs with Burgers vectors normal to the plane of sample surface. Assuming that the injected dislocation loops are stored in a hemisphere under the contact perimeter, they found that the density of GNDs is proportional to the reciprocal of indentation depth.

Nix and Gao used the Tabor's finding that the indentation hardness is a measure of the yield stress of the metal, the von Mises yield criterion connecting the yield stress with the critical resolved shear stress, and the Taylor's relation stating that the shear strength is proportional to the square root of the dislocation density.

Expressing the total dislocation density as the sum of densities of statistically stored and geometrically necessary dislocations, Nix and Gao finally found that

$$\frac{H}{H_0} = \sqrt{1 + \frac{h^*}{h}} . \qquad (3)$$

Here H_0 is the hardness that would arise from the statistically stored dislocations alone, and h^* is a length that characterizes the depth dependence of the hardness.

As the indenter penetrates the solid solution, it not only produces and emites GNDs, but it also "picks up" the solute atoms from the indent volume. The solute atom either remains "stuck" at the indenter's surface (with probability p^*), or leaves the surface (with probability $p^{**}=1-p^*$) and diffuses into indenter's vicinity. The solute atoms "stuck" at the indenter change its effective shape and size and thus modify the density of GNDs. The solute atoms diffused into indenter's vicinity enhance local concentration of solid solution and thus enhance the solid solution strengthening.

Because two strengthening mechanisms take place, the Taylor's relation for dislocation strengthening is replaced by the expression[3]

$$Y = k_s c^{1/2} + k_d \rho^{1/2}. \tag{4}$$

Here k_i are particular strengthening coefficients, c is the concentration of solute atoms, and ρ is the total dislocation density (the sum of the statistically stored and geometrically necessary dislocations).

Incorporating the above mentioned into the Nix and Gao model, the following relation for the indentation hardness was found:

$$H = H^* \sqrt{1 + \left(1 + p^* c\right)\frac{h^*}{h}} + H^{**} \sqrt{c} \sqrt{1 + p^{**} \frac{h}{h^{**}}} \tag{5}$$

Here h^*, h^{**} are two length scale parameters, H^* is the hardness resulting from the statistically stored dislocations alone, H^{**} is the parameter quantifying the contribution of solid solution.

3. Results and discussion

The changes in material's strength as detected by microindentation are explained in terms of local strain and solid solution hardening. The strain hardening decreases and the solid solution hardening increases with the indentation depth. So the former dominates for lower indentation depths, while the latter prevails for higher indentation depths. For a pure metal ($c=0$) only the strain hardening takes place and the relation (*5*) reduces to that of Nix and Gao (*3*). In this case the indentation hardness monotonously decreases with increasing indentation depth. For a solid solution, the indentation hardness firstly decreases, reaches the minimum, and then slightly increases with increasing indentation depth.

Fig. 1 presents the microhardness of materials made from iron powder coated with 12 wt.% of copper[4]. The data were extracted from the load-displacement curves, measured by the TTX-NHT apparatus with diamond Berkovich tip. The sinusoidal/cyclic mode with the maximum load of 100 mN was chosen. Solid points are for green sample, that is practically for a pure iron. The hard-

ness values monotonously decrease. The empty points are for sintered sample, that is practically for a solid solution. The hardness values firstly decrease and then slightly increase. This qualitatively agrees with the theoretical results.
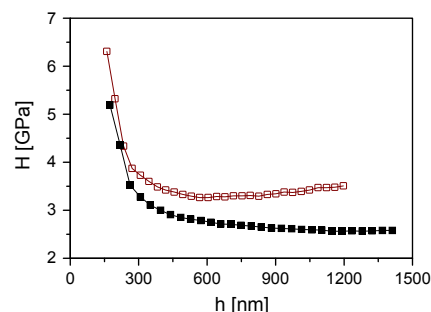

Fig. 1. **Typical curves for indentation hardness as function of penetration depth for samples prepared from 12 wt.%Cu coated iron powders: ■ sample in a "green" state, □ sintered at 1120 °C**

4. Conclusion

The relation for the micro-indentation hardness of solid solutions was obtained theoretically. The results qualitatively agree with the first data obtained for samples from copper-coated iron powders (green as well as sintered).

The applicability of relation (*5*) is now intensively tested on a series of various sintered samples.

REFERENCES
1. Tabor D.: Philosofical Magazine A *74*, 1207 (1996).
2. Nix W.D., Gao H.: J. Mech. Phys. Solids *46*, 411 (1998).
3. Soboyejo W.: „*Mechanical Properties of Engineered Materials*" (Marcel Dekker, Inc., 2003)
4. Kupková M., Kupka M., Strobl S., Hvizdoš P.: Chem. Listy *105*, s826 (2011).

M. Kupková[a] and M. Kupka[b] (*[a] Institute of Materials Research of SAS, Košice, [b] Institute of Experimental Physics of SAS, Košice, SR*): **Size-Dependent Microhardness of Two-Component Sintered Materials**

Nix and Gao model is modified to account for the micro-indentation of solid solutions. The changes in hardness are explained in terms of local dislocation strengthening due to geometrically necessary dislocations and local solid solution strengthening due to solute atoms transferred from indent volume to its vicinity. There is a qualitative agreement between obtained theoretical relation and first experimental data for sintered iron-copper samples.